World Scientific
www.worldscientific.com

Real-time co-registered photoacoustic and ultrasonic imaging for early endometrial cancer detection driven by cylindrical diffuser

Yongping Lin*,†, Peter Andreae‡, Zhifang Li*, Jianyong Cai* and Hui Li*,§

*College of Photonic and Electronic Engineering
Fujian Normal University
Fujian Provincial Key Laboratory of Photonic Technology
Fujian Provincial Engineering Technology Research Center
of Photoelectric Sensing Application
Key Laboratory of Optoelectronic Science and Technology for Medicine
Ministry of Education, Fuzhou 350007, Fujian, P. R. China

†Xiamen University of Technology
School of Optoelectronic and Communication Engineering
Xiamen 361024, Fujian, P. R. China

‡School of Engineering and Computer Science
Victoria University of Wellington
P.O. Box 600, Wellington, New Zealand
§hli@fjnu.edu.cn

In illuminating tissues, a cylindrical diffuser (CD) has an advantage over regular laser sources due to its ability to illuminate a larger volume of the target tissue. This paper presents a co-registered large volume photoacoustic (PA) and ultrasonic (US) imaging for early endometrial cancer (EEC) detection using CD. It has the advantage that the US imaging system is outside the body and only the PA excitation device is inside the body, which makes the system more efficient and less invasive for EEC detection. The paper reports on two sets of experiments. The first set produced real-time PA images of blood vessel phantom. The second set demonstrated the imaging of pig uterus *ex vivo*. The results show that the system has the potential for imaging and characterizing of EEC.

Keywords: Endometrial cancer; cylindrical diffuser; photoacoustic imaging.

§Corresponding author.

1. Introduction

Cancer of the uterine corpus is often referred to as endometrial cancer because most cases (92%) occur in the endometrium (lining of the uterus).[1] It is the most common female pelvic malignancy, with 63,230 cases estimated to be diagnosed in the United States in 2018 and 11,350 deaths expected.[2] Moreover, cancer of the uterine corpus (body of the uterus) is the fifth most common cancer for women and has a significant upward trend in age-standardized incidence rates in China.[3] Worldwide, cancer of the uterine corpus is more frequently diagnosed in developed countries than developing countries.[4] The pathologic condition is staged with the International Federation of Gynecology and Obstetrics (FIGO) system.[5] There are four stages for the cancer of the endometrium. In stage I — early or localized cancer of the endometrium — the tumor is confined to the corpus uteri. The 5-year overall survival rate for women with endometrial cancer is 80% to 90% for patients with stage I endometrial cancer, 60% to 80% for stage II, and widely divergent for stage III (30% to 80%), because of the diverse disease extent for tumors classified as FIGO stage III.[6] Technology capable of reliably diagnosing endometrial cancer in earlier stages or before the development of invasive disease could reduce the mortality and the large economic impact of this disease. Stage I is subclassified into stage IA (invasion of less than half of the myometrium) and stage IB (invasion of at least half of the myometrium). Most clinicians agree that the only candidates for conservative management of endometrial cancer are women with anticipated stage IA.[7] Therefore, we focused on diagnosis of stage I endometrial cancer in this paper.

The main tests for diagnosing cancer of the uterus are transvaginal ultrasound (US), magnetic resonance imaging (MRI), computed tomography (CT), hysteroscopy and biopsy.[8] US is limited by the overlapping acoustic characteristics of benign and malignant solid lesions.[9] MRI and CT are effective, but very expensive. Hysteroscopy and biopsy are invasive and increase the patient's mental burden. Photoacoustic (PA) imaging is a promising technique that complements US and is able to distinguish benign from malignant tumors. PA imaging systems are considerably less expensive than conventional MRI and CT imaging systems and show promise for real-time clinical applications. Recently, Nie *et al.*[10] demonstrated the PA microscopy system with synergistic theranostic strategy to be a multiplexing platform for tumor diagnosis at a very early stage. Lv *et al.*[11] applied a hemispherical PA imaging system for imaging of the mouse heart. Nevertheless, these systems could only be used in small organs. Wang *et al.*[12] presented simultaneous PA and US dual-mode endoscopy and showed its ability to image internal organs *in vivo*, thus illustrating its potential clinical application. Salehi *et al.*[13] presented a hand-held transvaginal probe suitable for co-registered PA and US imaging of ovarian tissue. However, imaging depth is only up to 30 mm which is not deep enough to be practical. Miranda *et al.*[14] presented a 2.92 mm diameter imaging probe which allows for entry into the human endometrial, in order to use PA imaging and high-resolution US to investigate the uterus. Liu *et al.*[15] developed a dual-modality endoscope composed of PA and hyperspectral imaging by a custom-mode Grin-lens with a diameter of 2 mm. However, they all used a focused US transducer which included optical fiber. That means both the PA excitation and capture are located inside the body. Since all the operations must be done inside the body, it is harder to control and more invasive. Our technique uses a small intrauterine PA excitation source but has the US transducers outside the body, which is easier to control and less invasive.

A small modification of current US scanners results in a shared detector platform (an array detector) that facilitates a natural integration of PA and US imaging, creating a hybrid imaging technique that combines functional (PA) and structural (US) information, fit for clinical translation.[16] Mitcham *et al.* investigated a PA image using an interstitial irradiation source with a clinical US system, which was shown to yield improved PA signal quality at distances beyond 13 mm.[17] However, the side-fire fibers or conical-tip fibers can not illuminate a whole tissue at the same time. Cyindrical diffusers (CD) are widely used in light therapies, such as photodynamic therapy,[18] photoimmunotherapy,[19] photothermal therapy,[20] and photocoagulation.[21] Kang *et al.* proposed a catheter-based CD as a feasible therapeutic tool to photocoagulate endometrial cell layers in an efficient and safe manner.[22] In previous work by our team, we proposed a PA method for the estimation and reconstruction of 3D light distribution produced by a CD in biological tissue.[23]

This paper describes a co-registered PA and US imaging system for EEC detection based on a CD.
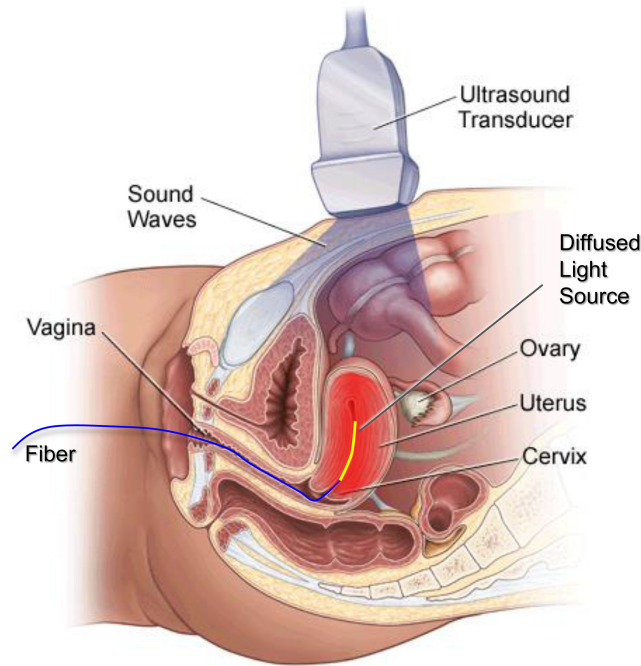
Fig. 1.   Schematic of co-registered PA and US imaging system for EEC.

A CD is inserted the uterus through the vagina and cervix to excite the PA signal; a clinical US transducer captures the signal outside the lower abdomen as shown in Fig. 1. Thus, only a thin fiber (diameter $\leq 1\,\text{mm}$) needs to reside inside the patient's body. This reduces the patient's discomfort and simplifies the surgery process. It is label-free and combines the good sensitivity and high contrast-to-noise ratio of PA imaging with the clear morphological features of US imaging in visualizing uterus lesions. It can illuminate almost the entire uterus at once which makes the imaging more efficient. The system is able to obtain PA and US cross-sectional images in real-time and reconstructs 3D images by transducer scanning. To demonstrate the initial feasibility of the system, a blood vessel phantom and an *ex vivo* pig uterus were imaged.

2.   Materials and Methods

When a short-pulsed laser beam irradiates the tissue, some of the light is absorbed by it. This causes a small transient temperature rise which is then further converted to a pressure rise via thermo-elastic expansion. The pressure rise is propagated as an ultrasonic wave, which can be detected by an US transducer as shown in Fig. 1. The initial local pressure (P_0) generated by the PA effect can be described as[24]

$$p_0 = \Gamma\eta_{\text{th}}\mu_a F, \tag{1}$$

where Γ is the dimensionless Grneisen coefficient; η_{th} is the percentage of absorbed light converted into heat; μ_a is the optical absorption coefficient (cm^{-1}) and F is the local laser fluence (J/m^2). Γ and η_{th} are usually approximated as constants, although they have been found to depend on the tissue type; After the generation of the initial pressure p_0, an acoustic wave starts to propagate in the material at the speed of sound. In US image reconstruction, the acoustic wave is first transmitted from the US transducer through a medium, with a specific velocity reflected at boundaries with impedance mismatching, and the backscattered sound is picked up by the US transducer. In clinical US systems, a conventional US dynamic receive-delay-and-sum algorithm is designed based on the entire acoustic time-of-flight (TOF) during this process, which can be formulated as[25]

$$t_{\text{US}}(r_F) = \frac{1}{c}\left(|r_T| + |r_R|\right), \tag{2}$$

where r_F is the focus point originating from the US image coordinates, r_T is the vector from the emitting element to the focal point, r_R is the vector from the focal point to the pickup element, and c is the

Y. Lin et al.

speed of sound. The acoustic TOF of PA signals is half that of US, because the acoustic wave is generated at the target by absorbing light energy, and the optical transmission side of time travel is negligible. Therefore, a PA dynamic receive-delay-and-sum algorithm was designed based on the acoustic TOF which can be formulated as

$$t_{\mathrm{PA}}(r_F) = \frac{|r_R|}{c}. \tag{3}$$

The co-registered PA and US imaging system can display the real-time US images and PA images at the same time by employing different receive-delay-and-sum algorithms.

2.1. *Monte Carlo simulations*

A 3D triangular mesh optical model of the uterus was built using the histological structure shown in Fig. 2. To investigate the light propagation beyond the uterus in an optically scattering medium, 3D Monte Carlo simulations were performed with a 66 mm × 66 mm × 84 mm homogeneous background tissue and a resolution cell of 0.3 mm. To investigate what shape of the diffused light source would provide the best illumination for the EEC detection, two main different shapes of the light source (cylinder, sphere) were implemented in the simulation. A cubical diffuser was considered but since it would have almost the same effect as the spherical diffuser (SD) due to their small size comparing to the uterine cavity, it was not implemented. A length of 2 cm and radius of 0.3 mm isotropic CD and a diameter of 0.6 mm isotropic SD

(a)   (b)

Fig. 2.   (a) Histological structure of the uterus and (b) 3D optical model of uterus.

were set in the center of the cavity ($z = -10$ mm), respectively. The azimuth angles of the two diffusers were from $0°$ to $360°$ and deflection angles were from $0°$ to $180°$. The penetration depth of light in the uterine wall is greatest at wavelength 800 nm,[26] so the wavelength was set to 800 nm. Simulated undiluted raw and homogenized milk (URHM) was filled into the uterine cavity to make the light distribution more homogeneous in the cavity of the uterus. Monte Carlo simulations were implemented using the latest published version of the Molecular Optical Simulation Environment (MOSE 2.3).[27]

The background optical properties of the absorption coefficient of $\mu_a = 1\,\mathrm{mm}^{-1}$, scattering coefficient of $\mu_s = 1e^{-5}\,\mathrm{mm}^{-1}$, anisotropy factor of $g = 1$ and refractive index of $n = 1$ and the uterine wall[26] of $\mu_a = 0.011\,\mathrm{mm}^{-1}$, $\mu_s = 9.1\,\mathrm{mm}^{-1}$, $g = 0.9$ and $n = 1.4$ were considered. In order to make a comparison, URH Milk[28] of $\mu_a = 0.014\,\mathrm{mm}^{-1}$, $\mu_s = 50\,\mathrm{mm}^{-1}$, $g = 0.96$ and $n = 1.34$ and air of $\mu_a = 1e^{-5}\,\mathrm{mm}^{-1}$, $\mu_s = 1e^{-5}\,\mathrm{mm}^{-1}$, $g = 1$ and $n = 1$ were filled in the uterine cavity, respectively. The total incident photon number was 500,000. Cartesian coordinates were used for the simulation.

MC simulations were implemented by laser energy (from 10^{-3} J to 1 J) of the CD at wavelength 800 nm to compare irradiated area. Meanwhile, to analyze the impact of the scattering coefficient to the light absorption distribution (LAD) in the uterine cavity, MC simulations were also implemented by the uterine model filled with different scattering coefficient (from $10^{-4}\,\mathrm{mm}^{-1}$ to $10^2\,\mathrm{mm}^{-1}$) materials at laser wavelength 800 nm.

2.2. *Experimental imaging setup*

The experimental system schematic is shown in Fig. 3(a). To obtain a laser wavelength of 800 nm, we used a pulsed Q-switched Nd:YAG laser (Surelite I-10, Continuum) at a wavelength of 532 nm, 6 ns pulse duration, and the 10 Hz repetition rate to pump a tunable optical parametric oscillator (Surelite OPO Plus, Continuum) at the wavelength of 800 nm. After exiting the optical parametric oscillator, the collimated light beam through the filter lens and plane-convex lens was sent to the optical fiber coupler. The radiation levels are maintained below the maximum permissible exposure (MPE) imposed by the American National Standards Institute (ANSI) for human skin.[29] Before entering the fiber, the laser beam's total input energy was
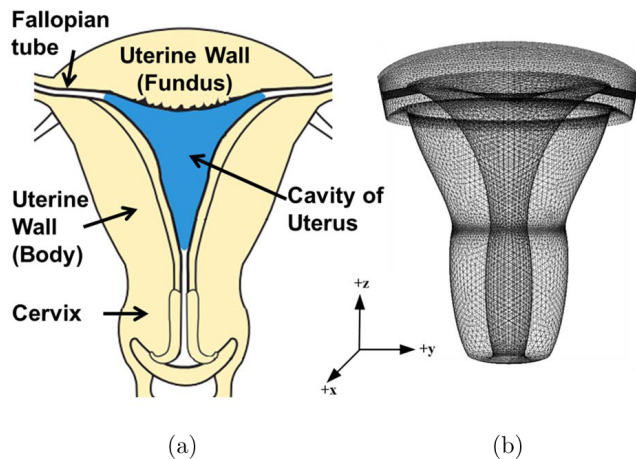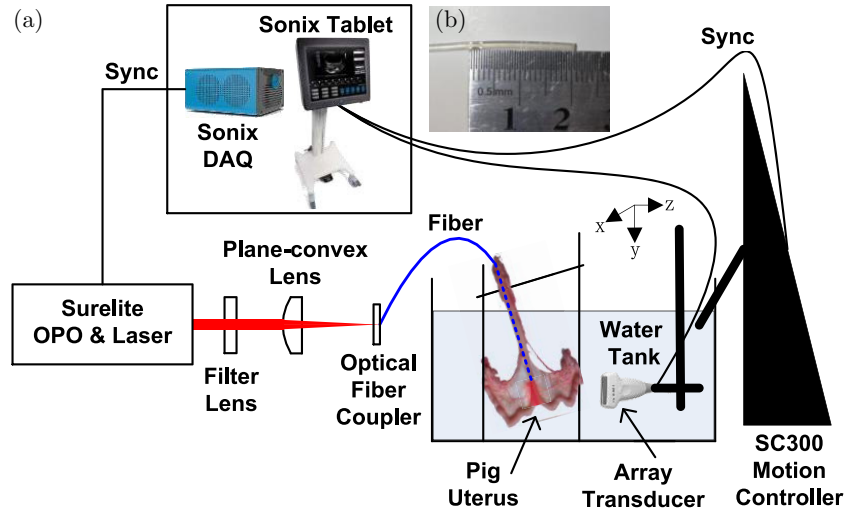
Fig. 3. (a) Experimental system schematic and (b) photograph of the CD.

150 mJ. The pulse light was then coupled to a fiber transmitter to the CD, as shown in Fig. 3(b) for the tissue illumination. The total radiated energy on the surface of the CD was approximately $4\frac{mJ}{cm^2}$ at 800 nm, well below the ANSI safety limit $31.70\frac{mJ}{cm^2}$ at 800 nm. The fiber was inserted into the sample, which was immobilized in the water tank. The linear array US transducer (0.3 mm pitch, 128 elements, 5–14 MHz bandwidth, 2–9 cm depth range) was also placed in the water tank, facing the sample, so as to capture the outgoing acoustic signal. The sampling rate for data acquisition was 40 MHz. The transducer was held in position by a precise XY-stage motion controller (SC300-2B, Zolix) which displaced it for scanning with a step size of 0.1 mm along the axis x. The whole system was controlled by a clinical US computer (Sonix Tablet) with an attached data acquisition device (Sonix DAQ) both manufactured by Ultrasonix. The pulsed laser sends synchronous pulse signals to the Sonix DAQ while emitting light, to make sure the Sonix Tablet can acquire the signal in time. After acquiring signals, the transducer is moved to a new position and the Sonix Tablet sends synchronous signals to the motion controller to acquire new signals. The data from the transducer is acquired by the Sonix tablet. The Sonix tablet is able to reconstruct the real-time 2D PA and US images by employing different receive-delay-and-sum algorithms. Furthermore, it can reconstruct 3D images by transducer scanning.

The spatial resolution of the system was described in our previous study.[30] The effective image rate of the real-time PA and US imaging system is limited to 10 images per second. However, the whole uterus is illuminated by a CD so that the light source doesn't need to adjust for finding a best illumination position. This saves lots of time and makes operation of the co-registered PA and US imaging system easier. That is to say, it reduces the patient's discomfort and simplifies the surgery process which would be result in faster implementation of the clinical using.

2.3. Phantom experiments

To demonstrate the system performance, A custom-made 6.8 mm height × 6.0 mm width uterine cavity model with two fallopian tubes, made of acrylonitrile butadience styrene (ABS) material and constructed with a 3D printer (the cavity surface was polished) as shown in Fig. 4(a) was employed. Uterine phantom was fabricated from a solution of agar powder and distilled water at a ratio of 2.5 g to 100 mL. At the beginning of the fabrication, the agar powder and distilled water were continuously stirred while heated. After mixing well, they were poured into a beaker with the uterine cavity model immobilized center inside. The uterine cavity model was taken out after solidification of the mixed solution. A photograph of the uterine phantom is shown in Fig. 4(b). A blood vessel was made by polyethylene tube (Inner diameter 0.5 mm, outer diameter 1 mm, and length 10 mm) filled with pig blood. The blood vessel was placed inside the uterine phantom which is about 1.5 cm away from the
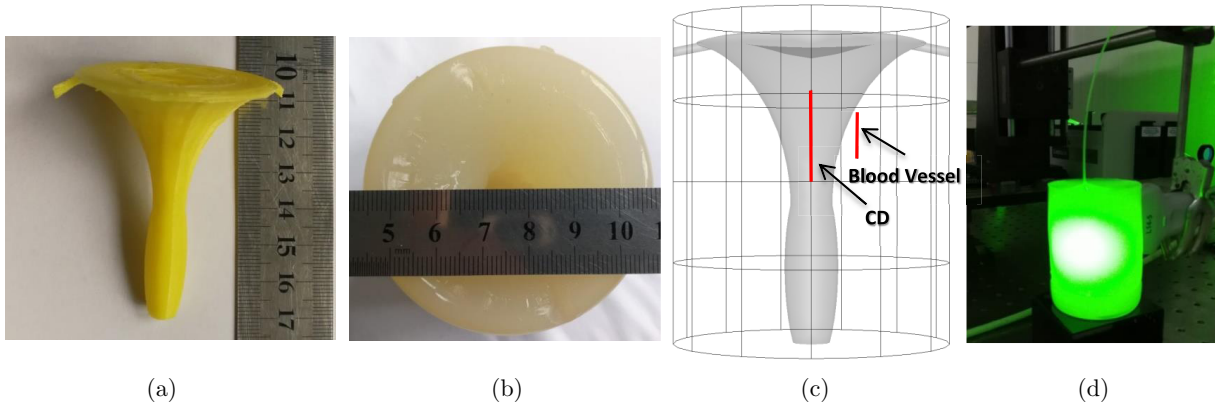
Fig. 4.   Photograph of (a) uterine cavity model, (b) uterine phantom, (c) a schematic diagram of the phantom experiment and (d) photograph of the uterine phantom experiment.

center of the uterine cavity as shown in Fig. 4(c). The transducer was aligned orthogonally to the blood vessel, in order to maximize the spatial resolution. Medical US couplant gel was put between the transducer and uterine phantom as shown in Fig. 4(d), to produce reliable nondestructive inspection result. We reconstructed 2D PA images at steps of 0.1 mm.

2.4.   *Pig uterus ex vivo experiments*

The top-view of a pig uterus sample is shown in Fig. 5(a). The region of interest (ROI) is a rectangular area of the sample (blue dotted rectangle). In order to simulate stage I of EEC, pig blood was injected into the pig uterus, which resulted in a blood-rich region of 5 mm in diameter, as shown on the right side in Fig. 5(a). Binder clips were used to prevent the sample floating up when securing the sample in the water tank. All the experiments were implemented by the experimental system described

before. A photograph was taken as shown in Fig. 5(b) by using 532 nm wavelength laser which is observable by human eye. The transducer was placed about 4 cm away from pig uterus. The experiment was first conducted to detect the PA signals of the pig uterus with nothing inside, then detect the PA signals of the pig uterus filled with enough Intralipid-20%, which is a reasonable substitute for URHM.[31]

3.   Results and Discussion

3.1.   *Simulation results*

LAD simulation results produced by CD or SD, filled with air or URHM, at 800 nm in yz-plane are shown in Fig. 6. The LAD values in Figs. 6(c) and 6(d) are bigger than the LAD values in Figs. 6(a) and 6(b) due to the uterine cavity filled with URHM. Comparing Figs. 6(a) and 6(b) or 6(c) and 6(d), slight LAD differences were obtained by
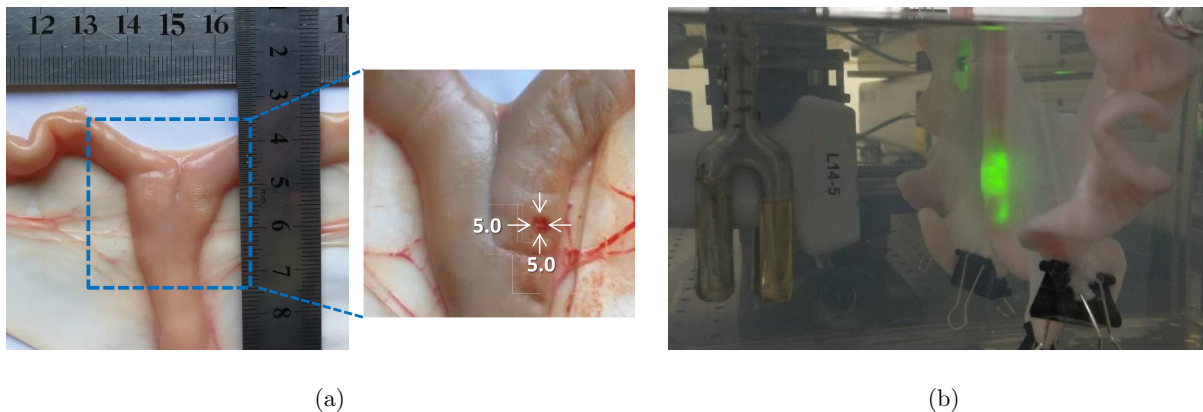

Fig. 5.   Photograph of (a) the pig uterus sample and (b) *ex vivo* pig uterus experiment.
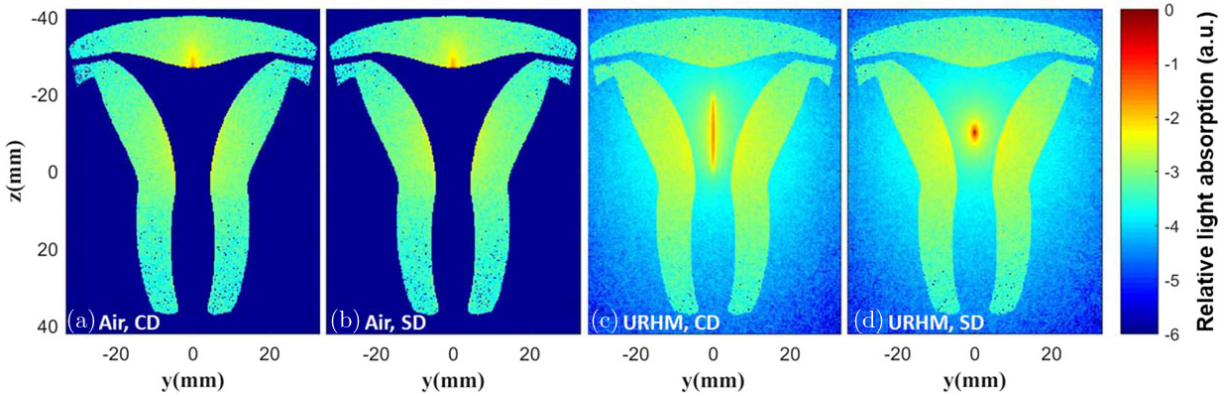
Fig. 6. LAD of the uterine model produced by CDL (a), (c) and SDL (b), (d) at wavelength 800 nm, respectively.

exciting the uterine model with CD and SD filled with air or URHM. However, the LAD differences of the uterine wall are hard to identify by the human eye. By contrast, the LAD profiles of the two laser sources can be easily observed. The LAD shape of CD is oval while the LAD shape of SD looks like circle. LAD of uterine model in xz-plane were not discussed because the 3D uterine model was designed in cylindrical symmetry along z-axis except for the fallopian tube. we have enough reason to believe that the same LAD of uterine model

would be found in xz-plane except for the fallopian tube which can only be observed in yz-plane.

In order to give a quantitative comparison of the irradiated range by the CD or SD filled with air or URHM at wavelength 800 nm, LAD through the center of the light sources ($z = -10$ mm) along the y-axis were analyzed. Figure 7(a) shows the LAD profiles of the uterine model. The average LAD values produced by the uterine model filled with URHM were higher than those of the uterine model filled with air. However, the differences between the
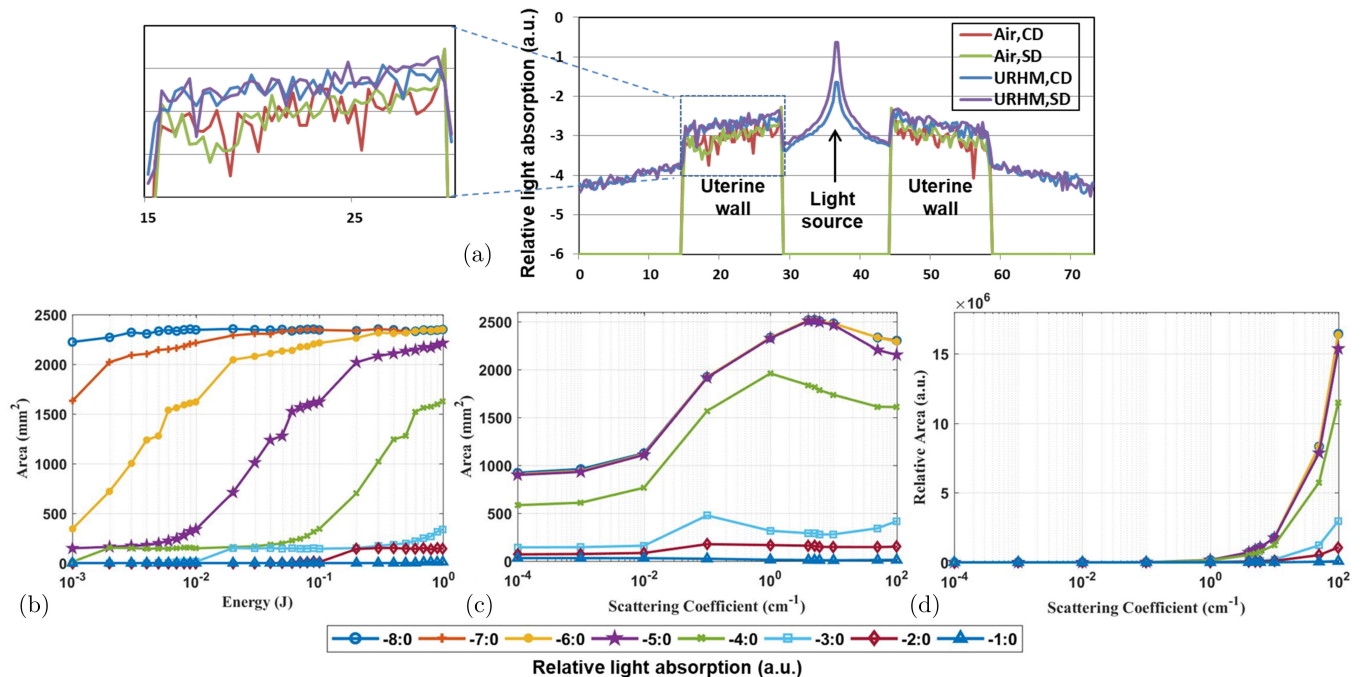

Fig. 7. (a) LAD of the uterine model at wavelength 800 nm through the center of light source, (b) irradiated area produced by the CD at different laser energy levels, (c) irradiated area and (d) relative irradiated area produced by the CD with different scattering coefficients.

LAD of the uterine model produced by CD and SD were hard to distinguish, no matter what the model was filled with. The LAD dropped down to almost the same value from the center to the uterine wall. That is to say, the shape of the light source is less important when the fiber is put in the center of a relatively large cavity. In real world, the size of the female uterine cavity ranges greatly and the geometry is complex; the upper uterine wall sticks to the lower uterine wall especially in post-menopause women. Under this consideration, we use the CD which can excite a larger area when the laser fiber is close to the uterine wall.

Higher laser energy results in higher signal-to-noise ratio (SNR). To get an acceptable PA SNR in the uterine wall, higher laser energy is recommended. Unfortunately, the higher laser energy is more costly and the maximum laser energy is also limited by the MPE level. The results of the irradiated areas in yz-plane ($x = 0\,\text{mm}$) produced by the CD at different thresholds of laser energy, from 10^{-3} J to 1 J, are shown in Fig. 7(b). By estimating an isotropic CD of $2\,\text{cm}$ in length and $0.3\,\text{mm}$ radius, according to the formula $2\pi * \text{radius}^2 + 2\pi * \text{radius} * \text{height}$ for the surface area of a cylinder, the surface area for the isotropic CD is $3.7756\,\text{cm}^2$. The maximum energy of the CD could be $119.68\,\text{mJ}$ at $800\,\text{nm}$ according to the MPE imposed by ANSI for human skin. By observing the energy of 10^{-1} J, the relative light absorption range from -5 to 0 starts to effect a large irradiated area. Obviously, only a small irradiated area is illuminated if the relative light absorption range is smaller than -5 to 0. In the experiments, the total radiated energy of the CD was approximately $15\,\text{mJ}$ at $800\,\text{nm}$, due to transmission loss and low conversion efficiency of the CD. For a range of -6 to 0, the effective irradiated area is about $1800\,\text{mm}^2$, which is more than two-thirds that of the whole uterine wall.

The results of the irradiated area in yz-plane ($x = 0\,\text{mm}$) produced by the CD with scattering coefficients from $10^{-4}\,\text{cm}^{-1}$ to $10^2\,\text{cm}^{-1}$ are shown in Fig. 7(c). It can be seen that there are peak values in every line. As we know, a higher scattering coefficient facilitates the light delivery in the tissue. However, higher scattering coefficients increase the chance of absorption. Thus, a relative irradiated area is defined as irradiated area times μ_s/μ_a. The results of the relative irradiated area are shown in Fig. 7(d). Significant increases were found in the relative irradiated area as the increase of scattering

coefficients exceed $1\,\text{cm}^{-1}$. In other words, the ratio between scattering coefficients and absorption coefficients has a large impact on the irradiated area. That is to say, a material which has an extremely small absorption coefficient and an extremely high scattering coefficient helps the light delivery in uterine cavity.

3.2. *Experimental results*

Figure 8 shows a sequence of five co-registered PA/US image frames of the uterine phantom arranged in time. The gray scale image is the US signal, whereas the color image is the PA signal. The images were obtained by mounting the imaging probe on a motion controller and then scanning across the uterine phantom. Frame 1 shows US trace of fiber and no PA trace, as the probe position is further away from the vessel and closer to the fiber. As the probe is continuously scanned across the uterine phantom, the subsequent frames begin to show more and more features, until reaching a certain position of the probe. Frames 2 and 4 show weak PA trace, whereas the strongest US trace of fiber found in Frame 2 and the best PA image contrast in Frame 3. The PA signal in Frame 3 was magnified, in which the dimensions of the vessel can be seen more clearly. The two lines seen are the front and back of the tube. The PA signal, in the time-domain from a cylindrical object like a tube, shows up as a characteristic "N-shape" pulse, when picked up with a very wide-band US transducer.[32] However, the transducer we used had a limited bandwidth, only the two positive and negative peaks of the N-shape pulse were observed. The length ($\approx 10\,\text{mm}$) of the detected vessel match the length of the vessel we made quite well.

Figures 9(a), 9(b) and 9(c) show co-registered 2D PA/US image of the *ex vivo* pig uterus experiments in different planes through the center of the tumor. Figure 9(d) shows reconstructed 3D co-registered PA/US pig uterus experimental images. The tumor can be observed in the corresponding place in the 2D images. Meanwhile, only the PA signal on the surface of the 3D image could be observed. Figures 10(a) and 10(b) show a sequence of eight continuous PA image frames of the pig uterus filled with air and URHM, respectively. The SNR was calculated as $\text{SNR} = 10\log_{10}(\frac{P_s}{P_n})$, where P_s is the average PA signal power inside the target, and P_n is noise power outside the region. The maximum SNR
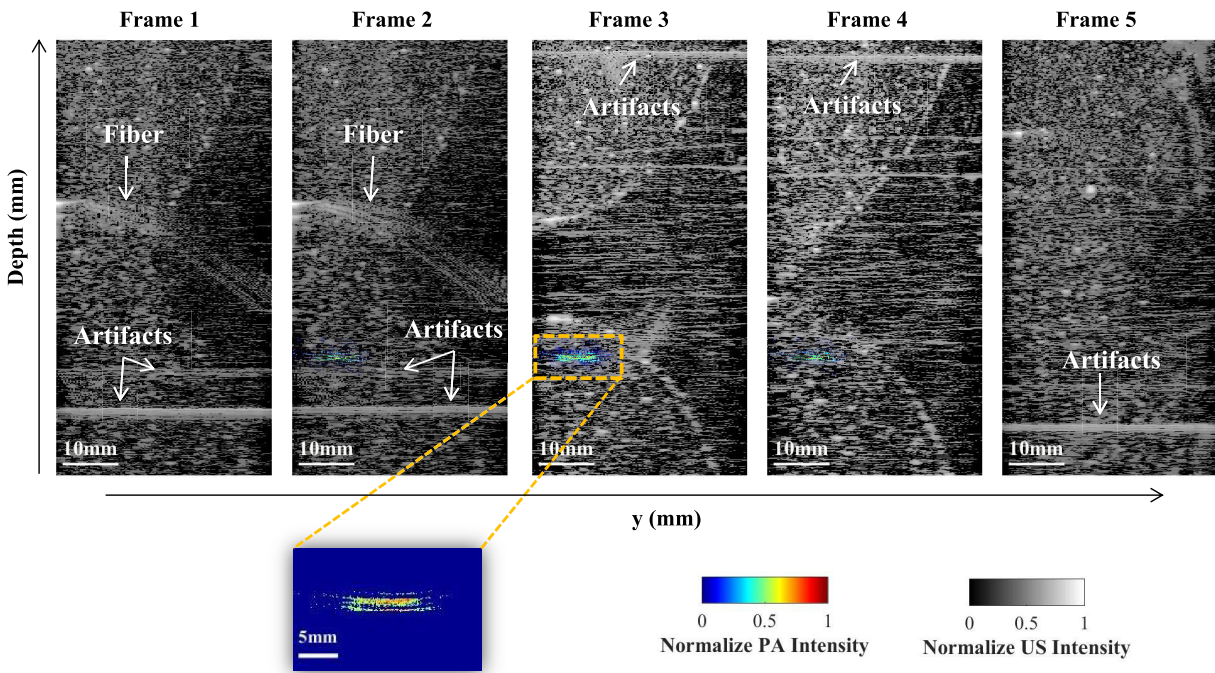
Fig. 8.   Co-registered PA/US images of the uterine phantom experiments.

of the pig uterus filled with air, occurring in Frame 4, is 19.87 dB, with an average SNR of 12.14 dB and a standard deviation SNR of 4.38. The maximum SNR of the pig uterus filled with URHM, occurring in Frame 4, is 15.03 dB, with an average SNR of 11.14 dB and a standard deviation SNR of 3.19. The lower standard deviation in the case of the pig uterus filled with URHM indicates that the URHM filling renders a more uniform light distribution.

In Frame 4, Fig. 10(a), a tumor of 5.1 mm in width and 6.8 mm in height was detected. The width is presented quite accurately, according to the tumor we made. However, the height is longer than the original tumor length. This is different
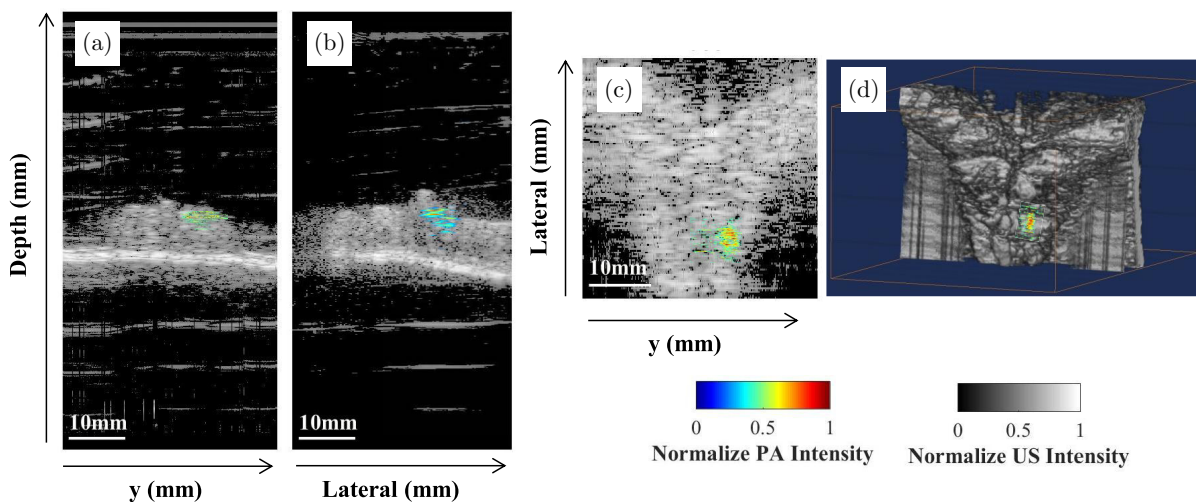

Fig. 9.   Co-registered PA/US images of the *ex vivo* pig uterus experiments along axis *y* (a) and along lateral direction, (b) through the center of tumor, (c) reconstructed co-registered 3D PA/US images of the *ex vivo* pig uterus experiments in *y*-lateral plane and (d) reconstructed co-registered 3D PA/US images of the *ex vivo* pig uterus.
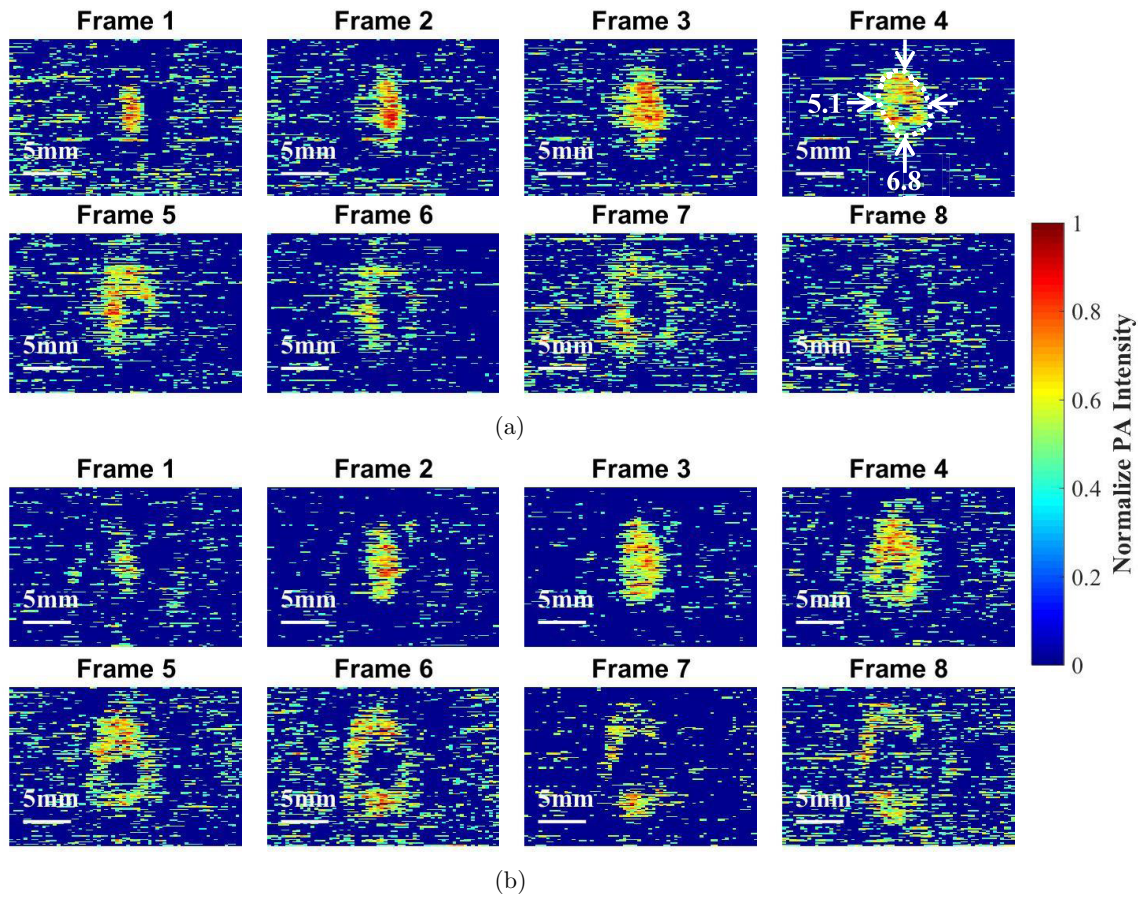
Fig. 10. Progression of PA image frames acquired in the pig uterus filled with (a) air and (b) URHM in xy plane.

from the original size because the tumor was vertically stretched by the use of binder clips. The PA signals of Frames 1 to 4 in Fig. 10(a) were gradually becoming larger, whereas the PA signals of Frames 5 to 8 were gradually spread out. This phenomenon was caused by the syringe being inserted only in half of the uterine wall. Same phenomenon can be observed Fig. 10(b).

3.3. Discussion

Co-registered PA/US imaging is good for improving early stage cancer detection. By filling the tissue with URHM and employing a DC for 360° irradiation, a larger volume of the tissue can be imaged at a time and provides a more uniform light distribution. The proposed system detects the tumor size quite accurately.

The maximum SNR of the pig uterus experiment is 19.87 dB, which is not very satisfactory in the detection of the PA signal, especially when the

tumor is located further away from the CD. Higher laser energy will result in a better SNR. However, the total radiated energy on the surface of the CD was approximately $4\frac{\text{mJ}}{\text{cm}^2}$ at 800 nm, due to transmission loss and low conversion efficiency in the CD. A better CD would increase the radiated energy and improve the SNR. Side-fire fiber tip and conical-tip fiber[17] could increase the radiated energy but they could not irradiate at 360°. Future work will investigate a fiber which has the best balance between the side fiber and irradiation angle. Another solution to enhance the SNR is using high PA contrast agents, such as nanoparticles. However, with current art technology, adding nanoparticles into the blood flow of uterus, an internal organ of human body, is not a feasible option.

4. Conclusion

In this paper, a real-time co-registered large volume PA and US imaging for EEC detection, driven by a

CD, has been demonstrated. This system is less invasive than other proposed PA/US systems because the US transducer is external and only the PA excitation device is internal. Furthermore, it simplifies the irradiation process by using a CD. Therefore, this imaging system presents promising potential in detection of EEC.

Conflict of Interest

The authors declare no conflict of interest.

Acknowledgments

References

1. American Cancer Society, *Cancer Facts & Figures 2017*, American Cancer Society (2017).
2. R. L. Siegel, K. D. Miller, A. Jemal, "Cancer statistics, 2018," *CA: A Cancer J. Clinicians* **68**(1), 7–30 (2018).
3. W. Chen, R.-S. Zheng, P. D. Baade, S. Zhang, H. Zeng, F. Bray, A. Jemal, X. Q. Yu, J. He, "Cancer statistics in China, 2015," *CA: A Cancer J. Clinicians* **66**, 115–132 (2016).
4. L. A. Torre, F. Bray, R. L. Siegel, J. Ferlay, J. Lortet-Tieulent, A. Jemal, "Global cancer statistics, 2012," *CA: A Cancer J. Clinicians* **65**, 87–108 (2015).
5. S. Pecorelli, "Corrigendum to Revised FIGO staging for carcinoma of the vulva, cervix, and endometrium," *Int. J. Gynecol. Obstetric.* **108**, 176–176 (2010).
6. C. L. Creutzberg, G. F. Fleming, *Endometrial Cancer*, pp. 1203–1229, Elsevier Inc. (2016).
7. C. Corzo, N. Barrientos Santillan, S. N. Westin, P. T. Ramirez, "Updates on Conservative Management of Endometrial Cancer," *J. Minimally Invasive Gynecol.* **25**, 308–313 (2018).
8. Cancer Council Australia, *Understanding Cancer of the Uterus*, March 2017 edn., Cancer Council Australia (2017).
9. M. Pramanik, Dual-modality thermoacoustic and photoacoustic imaging, Ph.D Thesis, Washington University in St. Louis (2010).
10. L. Nie, P. Huang, W. Li, X. Yan, A. Jin, Z. Wang, Y. Tang, S. Wang, X. Zhang, G. Niu, X. Chen, "Early-Stage imaging of nanocarrier-enhanced chemotherapy response in living subjects by scalable photoacoustic microscopy," *ACS Nano* **8**, 12141–12150 (2014).
11. J. Lv, Y. Peng, S. Li, Z. Guo, Q. Zhao, X. Zhang, L. Nie, "Hemispherical photoacoustic imaging of myocardial infarction: *In vivo* detection and monitoring," *Euro. Radiol.* **28**, 2176–2183 (2018).
12. J.-M. Yang, C. Favazza, R. Chen, J. Yao, X. Cai, K. Maslov, Q. Zhou, K. K. Shung, L. V. Wang, "Simultaneous functional photoacoustic and ultrasonic endoscopy of internal organs *in vivo*," *Nat. Med.* **18**, 1297–1302 (2012).
13. H. S. Salehi, P. D. Kumavor, H. Li, U. Alqasemi, T. Wang, C. Xu, Q. Zhu, "Design of optimal light delivery system for co-registered transvaginal ultrasound and photoacoustic imaging of ovarian tissue," *Photoacoustic.* **3**(3), 114–122 (2015).
14. C. Miranda, J. Barkley, B. S. Smith, "Intrauterine photoacoustic and ultrasound imaging probe," *J. Biomed. Opt.* **23**, 1 (2018).
15. N. Liu, S. Yang, D. Xing, "Photoacoustic and hyperspectral dual-modality endoscope," *Opt. Lett.* **43**, 138 (2018).
16. S. Zackrisson, S. M. W. Y. Van De Ven, S. S. Gambhir, "Light in and sound out: Emerging translational strategies for photoacoustic imaging," *Cancer Res.* **74**, 979–1004 (2014).
17. T. Mitcham, K. Dextraze, H. Taghavi, M. Melancon, R. Bouchard, "Photoacoustic imaging driven by an interstitial irradiation source," *Photoacoustic.* **3**(2), 45–54 (2015).
18. M. D. Stringasci, T. C. Fortunato, L. T. Moriyama, J. D. V. Filho, V. S. Bagnato, C. Kurachi, "Interstitial PDT using diffuser fiberinvestigation in phantom and *in vivo* models," *Lasers Med. Sci.* **32**, 1009–1016 (2017).
19. S. Okuyama, T. Nagaya, K. Sato, F. Ogata, Y. Maruoka, P. L. Choyke, H. Kobayashi, "Interstitial near-infrared photoimmunotherapy: Effective treatment areas and light doses needed for use with fiber optic diffusers," *Oncotarget* **9**, 11159–11169 (2018).
20. Z. Li, H. Chen, F. Zhou, H. Li, W. Chen, "Interstitial photoacoustic sensor for the measurement of tissue temperature during interstitial laser phototherapy," *Sensors* **15**, 5583–5593 (2015).
21. M. Ahn, Y.-G. Chae, J. Hwang, Y.-C. Ahn, H. W. Kang, "Endoluminal application of glass-capped diffuser for *ex vivo* endovenous photocoagulation," *J. Biophotonic.* **10**, 997–1007 (2017).
22. H. W. Kang, J. Kim, J. Oh, "Enhanced photocoagulation with catheter-based diffusing optical device," *J. Biomed. Opt.* **17**, 118001 (2012).
23. W. Xie, Y. L. Yubin Liu, Z. L. Zhifang Li, H. L. Hui Li, "Reconstruction of 3D light distribution produced by cylindrical diffuser in deep tissues based on photoacoustic imaging," *Chin. Opt. Lett.* **12**(5), 051702–51705 (2014).

24. L. Wang, C. Zhang, L. V. Wang, "Grueneisen relaxation photoacoustic microscopy," *Phys. Rev. Lett.* **113**, 174301 (2014).

25. H. K. Zhang, M. A. L. Bell, X. Guo, H. J. Kang, E. M. Boctor, "Synthetic-aperture based photoacoustic re-beamforming (SPARE) approach using beamformed ultrasound data," *Biomed. Opt. Exp.* **7**, 3056 (2016).

26. P. M. Ripley, J. G. Laufer, A. D. Gordon, R. J. Connell, S. G. Bown, "Near-infrared optical properties of *ex vivo* human uterus determined by the Monte Carlo inversion technique," *Phys. Med. Biol.* **44**, 2451–2462 (1999).

27. S. Ren, X. Chen, H. Wang, X. Qu, G. Wang, J. Liang, J. Tian, "Molecular Optical Simulation Environment (MOSE): A platform for the simulation of light propagation in Turbid media," *PLoS ONE* **8**, e61304 (2013).

28. B. Aernouts, R. Van Beers, R. Watté, T. Huybrechts, J. Jordens, D. Vermeulen, T. Van Gerven, J. Lammertyn, W. Saeys, "Effect of ultrasonic homogenization on the Vis/NIR bulk optical properties of milk," *Colloid. Surfaces B: Biointerfaces* **126**, 510–519 (2015).

29. American National Standards Institute, *American National Standard for the Safe Use of Lasers: ANSI Z136.*, pp. 1–2000, American National Standards Institute (2000).

30. Y. Lin, Z. Li, Z. Li, J. Cai, H. Wui, H. Li, "Real-time photoacoustic and ultrasonic dual-modality imaging system for early gastric cancer: Phantom and *ex vivo* studies," *Opt. Comm.* **426**, 519–525 (2018).

31. R. Michels, F. Foschum, A. Kienle, "Optical properties of fat emulsions," *Opt. Exp.* **16**, 5907 (2008).

32. P. D. Kumavor, U. Alqasemi, B. Tavakoli, H. Li, Y. Yang, X. Sun, E. Warych, Q. Zhu, "Co-registered pulse-echo/photoacoustic transvaginal probe for real time imaging of ovarian tissue," *J. Biophotonic.* **6**, 475–484 (2013).